Check for updates

Advanced Engineering Materials

ADVANCED ENGINEERING MATERIALS
www.aem-journal.com

RESEARCH ARTICLE OPEN ACCESS

Hydrogen-Assisted Fracture of Iron-Based Fe–Ni–Al Alloys

Nataliya Yadzhak[1,2] | Olha Zvirko[3] | Rostyslav Leshchak[4] | Hryhoriy Nykyforchyn[3]

[1]Metals and Alloys, Faculty of Engineering Science, University of Bayreuth, Bayreuth, Germany | [2]Chair of Mechanics, Faculty of Mechanics and Mathematics, Ivan Franko National University of Lviv, Lviv, Ukraine | [3]Department of Diagnostics of Materials Corrosion-Hydrogen Degradation, Karpenko Physico-Mechanical Institute of the National Academy of Sciences of Ukraine, Lviv, Ukraine | [4]Department of Strength of Materials and Structures in Hydrogen-Containing Environments, Karpenko Physico-Mechanical Institute of the National Academy of Sciences of Ukraine, Lviv, Ukraine

Correspondence: Nataliya Yadzhak (nataliya.yadzhak@uni-bayreuth.de)

Received: 30 November 2025 | **Revised:** 26 March 2026 | **Accepted:** 13 April 2026

Keywords: body-centered cubic alloys | Fe-based alloys | hydrogen embrittlement | mechanical properties | superalloys

ABSTRACT

Precipitate-strengthened Fe-based alloys, often referred to as body-centered cubic superalloys, are considered as promising candidates for elevated-temperature applications up to 700°C due to their low density, cost efficiency, and favorable mechanical performance in this temperature range. While the fundamental properties of the Fe–Ni–Al system are well studied, their behavior under hydrogen-containing environments remains insufficiently understood, despite the high relevance of hydrogen-rich and H_2O-bearing atmospheres in next-generation energy systems. Given the intrinsic room-temperature brittleness of Fe-rich Fe–Ni–Al alloys and the ability of hydrogen to act as an embrittling agent, systematic investigation of hydrogen–alloy interactions is essential. This study addresses this gap by examining the influence of hydrogen on Fe-rich compositions within the Fe–Ni–Al system, providing insights into their mechanical response after hydrogen charging. Single-phased and two-phased precipitate-strengthened Fe–Ni–Al alloys are compared in terms of mechanical properties after hydrogen charging, with the two-phase alloys showing over 50% better strength in both the reference and charged states, despite their brittle behavior. The variety of investigated charging modes allows achieving a range of hydrogen concentrations that are related to the failure stress of the alloys.

1 | Introduction

In most challenging applications, Ni-based superalloys are the material of choice due to their excellent properties, such as good creep and high temperature resistance, combined with corrosion and fatigue resistance [1, 2]. Attempting to go beyond Ni-based superalloys, aluminides were developed for high-temperature applications [3]. By possessing higher melting temperatures, lower densities, better oxidation resistance, lower ductile to brittle transition temperatures, comparable thermal expansion coefficients to metals, and being inexpensive, they show advantages compared to Ni-based superalloys [3]. However, their insufficient performance is attributed to low creep and strength resistance at high temperatures, as well as low fracture toughness and ductility at low temperatures [3].

To address these challenges, ferritic alloys, or ferritic superalloys, as they are often referred to in literature [4, 5], have been developed, following the beyond Ni-based superalloy approach. The distinctive feature of this class of alloys is their matrix-precipitate microstructure, mimicking the microstructure of Ni-based superalloys with an iron matrix and aluminide precipitates. In contrast to the face-centered cubic (fcc) microstructure of Ni-based superalloys, the Fe-based alloys possess the body-centered cubic (bcc) microstructure [5], belonging to the growing class of bcc-superalloys [6, 7].

Ferritic superalloys are a promising class of high-temperature alloys due to their low density, low costs, and good mechanical properties at elevated temperatures up to 700°C. Possible interesting applications are power-generating turbines and steam turbines [8, 9]. However, with respect to the current developments,

This is an open access article under the terms of the Creative Commons Attribution License, which permits use, distribution and reproduction in any medium, provided the original work is properly cited.

© 2026 The Author(s). *Advanced Engineering Materials* published by Wiley-VCH GmbH.

peripheral components might no longer be exposed to mainly fossil fuel combustion atmospheres but rather to H_2-containing atmospheres [10]. Additionally, hydrogen can be incorporated into the material during H_2O-exposure. With respect to this, fundamental investigations have to be conducted on the stability of ferritic superalloys to such conditions to further identify superior – or also inferior – properties compared to commonly used materials for these applications, such as Ni-based alloys or austenitic steels.

Although the operation of applications in hydrogen-rich environments often involves high temperatures, investigations of hydrogen influence at room temperature are of significant importance, as the presence of residual stresses arising during shutdowns cannot be excluded. This is evidenced by cases in which failure occurred not during operation, but after the structure had been taken out of service. The practice of high-temperature operation of thermal equipment shows that cracking is significantly influenced by shutdowns during operation [11]. In addition, residual stresses are known to develop as a result of hydrogen charging. A notable example is hydrogen-induced cracking (HIC), which can occur in the absence of externally applied loads and is driven by stresses generated during hydrogen uptake. The manifestation of the HIC mechanism in pipeline steels is accompanied by crack initiation and propagation, as well as delamination [12]. Regardless of the specific mechanism of hydrogen action, it affects the fracture behavior of a material, underscoring the practical importance of such evaluations under room-temperature conditions.

The current paper focuses on the investigation of the Fe–Ni–Al system as a representative of the ferritic bcc-alloys in relation to the influence of hydrogen at room temperature. The general properties, phase equilibria, and phase diagrams, crystallographic and thermodynamic features of the Fe–Ni–Al system are widely studied [13–21]. The wide range of the existing and potential applications of the Fe–Ni–Al system is attributed to its desired properties, such as high melting point and good oxidation resistance [19], as well as an attractive price. However, the major drawbacks of this group of alloys are enhanced brittleness and poor ductility at room temperature [19, 22]. Since hydrogen also causes embrittlement, the effect of hydrogen on such sensitive materials requires fundamental understanding. As one of the widely spread external environments, hydrogen can be taken up by metals, diffuses, and accumulates in metallic materials, influencing their properties, microstructure, and phase equilibrium [23–29]. The hydrogen influence differs depending on material, microstructure, and type of specimens, causing hydrogen embrittlement; however, in some cases, the reverse hydrogen effect has been observed [30].

However, little study exists that systematically describes the Fe-rich Fe–Ni–Al behavior in a hydrogen medium. Of the three elements of the Fe–Ni–Al system, iron was the first element where hydrogen embrittlement was ever observed in 1874 [31], and the iron–hydrogen interaction mechanism has been extensively studied since then. Since the hydrogen effect is related to alloy composition, microstructure, and crystal structure, the addition of Ni and Al affects the hydrogen embrittlement process. For austenitic steels, it was observed that Ni-alloyed steels show a strong decrease in ductility under electrochemical hydrogen charging [28, 32], while presenting little hydrogen embrittlement under gaseous charging [33]. In addition, alloying Fe-based steels with aluminum facilitates hydrogen embrittlement as compared to the corresponding unalloyed material [28, 32]. In contrast to Ni-based alloys and austenitic steels (fcc crystal structure), which are presently used in a lot of high temperature applications, ferritic steels (bcc crystal structure) are more sensitive to small amounts of hydrogen and microstructural variations [34].

The effect of hydrogen on metallic materials and the hydrogen embrittlement process are usually studied using a combination of different approaches [24]. Mechanical investigations are conducted at low deformation rates to account for hydrogen diffusion during the test, so that slow strain rate testing and bending testing are generally used [35, 36]. Microstructural approaches include fracture surface examination, analysis of microstructure and phase composition of the materials, and their influence on the hydrogen-related behavior [37, 38]. Besides, the hot and melt gas extraction is applied to determine the hydrogen concentration [39], thermal desorption analysis allows investigating hydrogen trapping and calculating the corresponding activation energy [39, 40], and hydrogen diffusion coefficients can be measured by hydrogen permeation tests [35, 41]. Advanced approaches include secondary ion mass spectroscopy [42] and atom probe tomography [43, 44] for mapping the spatial distribution of hydrogen, as well as decoration techniques, such as the hydrogen microprint technique [37, 45], silver decoration, and Kelvin probe [46] to locate hydrogen on the sample surface.

The present study focuses on fundamental research on the influence of hydrogen on ferritic bcc Fe–Ni–Al alloys by investigating their mechanical properties at room temperature. This study combines mechanical, microstructural, and thermal approaches to investigate the hydrogen effect from a mechanical perspective.

2 | Experimental Section

2.1 | Materials Manufacturing

The studied alloys are Fe-based, alloyed with nickel and aluminum, while both Ni and Al content lie in the range of 10%–25%. In this paper, the following three alloys are considered: Fe65%-Ni10%-Al25%, Fe65%-Ni15%-Al20%, Fe65%-Ni17%-Al18% (in at-%). The alloys were manufactured from raw elements with a purity of over 99.95% (Fe: 99.97% purity produced by ThermoScientific, Ni: 99.95% purity by HMW Hauner GmbH &Co.KG; Al: 99.99% purity by Chempur Feinchemikalien und Forschungsbedarf GmbH) using a vacuum induction melting furnace. The composing elements were melted in a zirconium oxide yttrium-stabilized crucible under vacuum to avoid oxidation of the elements and poured into a copper mold. As a result, rectangular ingots with a cross-section of 19×29 mm were obtained.

In order to achieve the desired matrix-precipitate microstructure, the manufactured alloys underwent a two-stage heat treatment process. First, the samples were homogenized by heating them up to the temperature of 1250°C and holding for 4 h, followed by aging at the temperature of 850°C for 5 h. The heat-treatment was conducted in a vacuum cold-wall furnace (XERION Advanced Heating Ofentechnik GmbH) under a vacuum atmosphere, which

15272648, 2026, 17, Downloaded from https://advanced.onlinelibrary.wiley.com/doi/10.1002/adem.202503163 by Universitaet Bayreuth, Wiley Online Library on [27/10/2026]. See the Terms and Conditions (https://onlinelibrary.wiley.com/terms-and-conditions) on Wiley Online Library for rules of use; OA articles are governed by the applicable Creative Commons License

allowed to avoid oxidation of the alloys at high temperatures during the process.

From the heat-treated alloys, samples were cut using electrical discharge machining (Cut 200 SP by AgieCharmilles). The obtained samples were ground using silicon carbide sandpapers up to 1200 grit and degreased with acetone, in order to remove the resultant oxide layer, eventual surface defects, and prepare the surface for hydrogen charging.

2.2 | Materials Characterization

The chemical composition of the obtained ingots was determined using micro X-ray fluorescence analysis (μXRF) (Orbis PC by Ametek) and presented in Table 1.

The microstructural analysis involves the characterization of the alloy microstructure using a scanning electron microscope (SEM, ZEISS CrossBeam 1540 EsB) equipped with secondary electron (SE) and backscatter electron (BSD) detectors. For the local chemical analysis, a ThermoFischer EDX detector was employed, while the phase analysis was performed by an X-ray diffractometer (Bruker D8).

2.3 | Hydrogen Charging

In order to introduce hydrogen into the samples, electrochemical hydrogen charging was used employing a self-built electrochemical cell. The charging was conducted at room temperature in an electrolyte consisting of an aqueous H_2SO_4 solution with pH 1 and 800 μg/l H_2SeO_4 as a charging promoter. A platinum mesh electrode was used as an anode, and the sample served as a cathode. During the charging process, the sample ($19 \times 6.5 \times 2$ mm) was fully immersed in the electrolyte. To investigate the material response to different hydrogen contents, the charging parameters of cathodic current density, j, and charging time, t, were varied. Constant current densities of 10 and 20 mA/cm^2 were applied for charging times between 24 and 96 h. Despite the partially severe charging conditions, they were chosen in a way that no blistering occurred due to charging.

The hydrogen concentration was determined by the hot gas extraction method using a LECO DH603 hydrogen concentration analyzer. Measurements were conducted for all hydrogen-charged specimens, the mass of the samples was 0.8 ± 0.05 g. During the analysis, the specimen was heated up to 1100°C, which is below the melting temperature of the alloys. The hydrogen present in the material can be classified into diffusible (mobile) and residual (strongly trapped) [25]. During the measurement at 1100°C, the trapped hydrogen is released, transforming into diffusible hydrogen and desorbing together with the diffusible hydrogen present at room temperature. This combined release is recorded as the total desorbed hydrogen. Thus, the integral hydrogen concentration is determined irrespective of its initial state at room temperature.

2.4 | Mechanical Testing

Mechanical properties of the alloys were evaluated through three-point bending testing and hardness measurements. The hardness measurements were conducted by Rockwell (HRC) according to DIN EN ISO 6508–1 [47] and microhardness by Vickers (HV 0.1) under the test force of 0.9807 N according to DIN EN ISO 6507–1 [48].

For the three-point bending tests, small specimens with dimensions of $19 \times 6.5 \times 2$ mm were used. For each case, the test was repeated a minimum of three times. The specimens were tested on the bending device with a former movement rate of 0.5 mm/min and a distance between the supports of 16 mm according to the DIN EN ISO 7438 [49]. The specimens were loaded until fracture, recording the force F – time t and deflection f – time t diagrams. Subsequently, considering the loading rate and the geometric parameters of the specimens, the recorded data were converted into a force F – deflection f diagram, as well as a stress σ – strain ε diagram. The stress σ on the stretched surface of the beam sample was determined by the formula

$$\sigma = \frac{3Fl}{2bh^2} \tag{1}$$

where b – is the width, l – the length, and h – the height of the test specimen.

Based on the maximal force F_{max} and deflection f_{max} values, Young's modulus E was calculated, and elastic deformation was determined as a relation between the tensile stress and the Young´s modulus.

3 | Results and Discussion

3.1 | Materials

Figure 1 presents the microstructure of heat-treated alloys, investigated by SEM. After solution heat treatment and aging, the $Fe_{65}Ni_{17}Al_{18}$ and $Fe_{65}Ni_{15}Al_{20}$ alloys possess a highly-resolved two-phased matrix-precipitate microstructure with an iron matrix and B2 NiAl precipitates (Figure 1a–d), which is in line with literature data [19, 21, 50]. The shape of precipitates in both alloys is

TABLE 1 | The nominal and measured (μXRF) composition of the investigated alloys.

	Nominal composition, at-%			Measured composition, at-%		
Alloy	**Fe**	**Ni**	**Al**	**Fe**	**Ni**	**Al**
$Fe_{65}Ni_{10}Al_{25}$	65	10	25	66.7 ± 0.9	9.5 ± 0.4	23.8 ± 1.7
$Fe_{65}Ni_{15}Al_{20}$	65	15	20	66.6 ± 1.3	14.3 ± 0.3	19.1 ± 0.9
$Fe_{65}Ni_{17}Al_{18}$	65	17	18	66.6 ± 0.9	16.2 ± 0.3	17.2 ± 1.0

15272648, 2026, 17, Downloaded from https://advanced.onlinelibrary.wiley.com/doi/10.1002/adem.202503163 by Universitaet Bayreuth, Wiley Online Library on [27/10/2026]. See the Terms and Conditions (https://onlinelibrary.wiley.com/terms-and-conditions) on Wiley Online Library for rules of use; OA articles are governed by the applicable Creative Commons License

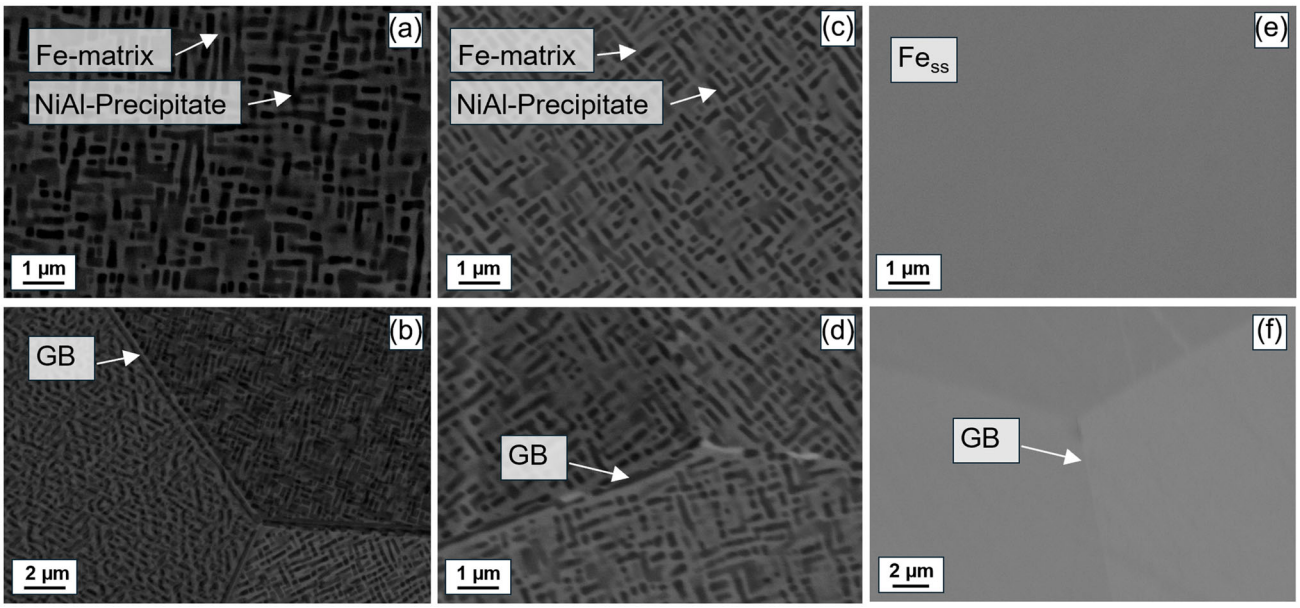


FIGURE 1 | Microstructure of $Fe_{65}Ni_{17}Al_{18}$ (a,b), $Fe_{65}Ni_{15}Al_{20}$ (c,d), and $Fe_{65}Ni_{10}Al_{25}$ (e,f) alloys. SEM images using a BSD.

rounded cuboids, which coarsened and coalesced into elongated rods. This resulted in the formation of plates and networks, creating a "maze-like" morphology, as also reported for Fe–Ni–Al–Cr alloys [51]. In the $Fe_{65}Ni_{17}Al_{18}$, the particle size ranges from 0.2 µm for cuboid precipitates to up to 2 µm for the coarsened particles, with an average spacing of 0.1 µm. For the $Fe_{65}Ni_{15}Al_{20}$ alloy, the precipitates are slightly smaller, ranging from 0.1 to 1 µm, with a spacing of 0.2 µm. The volume fraction of precipitates in $Fe_{65}Ni_{17}Al_{18}$ is approximately 10% higher than in the $Fe_{65}Ni_{15}Al_{20}$ alloy. The third alloy, $Fe_{65}Ni_{10}Al_{25}$, is single-phased B2-(Fe, Ni)Al [18] (Figure 1e). Both two-phase alloys have comparable grain sizes, with $Fe_{65}Ni_{17}Al_{18}$ possessing slightly larger grains, while the grain size of $Fe_{65}Ni_{10}Al_{25}$ is almost two times larger. The SEM-micrographs additionally show the presence of matrix-precipitate sandwich structures along grain boundaries (GB) (Figure 1b,d) for the two-phase alloys, which have also been reported for other ferritic superalloys [5, 52].

3.2 | Mechanical Characterization

3.2.1 | Hardness and Microhardness

In Table 2, the hardness (HRC) and microhardness (HV 0.1) values of the studied alloys are presented for the reference state and the hydrogen-charged samples. Vickers hardness HV 0.1 for a range of compositions in the Fe–Ni–Al system has previously been reported by Dorantes-Rosales et al. [21] and Contreras-Piedras et al. [19]. Increasing Al and Ni contents were observed to lead to higher hardness due to a higher volume fraction of precipitates, which, however, also results in reduced coarsening resistance of precipitates [19, 21, 53]. In this respect, a maximal threshold value of 15 at-% Ni and 15 at-% Al was proposed for optimal hardness and coarsening properties [19, 21]. At higher Ni and Al contents, the observed hardness decrease is attributed to precipitate coarsening and interconnection [53] as well as to the "splitting effect" of the hard B2 phase [54].

For all investigated alloys, charging exhibited no influence on the HRC hardness. However, microhardness was affected by hydrogen charging, although to a different extent: the harder single-phased alloy $Fe_{65}Ni_{10}Al_{25}$ showed a slight increase in HV 0.1, while the two-phase alloys $Fe_{65}Ni_{15}Al_{20}$ and $Fe_{65}Ni_{17}Al_{18}$ with initially lower microhardness exhibited a stronger increase.

Taking into account the high diffusivity of hydrogen in bcc alloys [29], as well as a prolonged charging time and small sample thickness, the hydrogen is considered to penetrate through the sample thickness during charging. Since the hardness measurements were conducted shortly after charging to minimize hydrogen effusion from the sample, a correlation can be made between the total hydrogen concentration and the surface hydrogen concentration.

Hydrogen-induced increase in micro- and nanohardness is widely reported for different materials [55–60]. The hardness

TABLE 2 | Hardness (HRC) and microhardness (HV 0.1) of alloys in the reference state and after charging at 20 mA/cm^2 for 24 h.

	$Fe_{65}Ni_{10}Al_{25}$		$Fe_{65}Ni_{15}Al_{20}$		$Fe_{65}Ni_{17}Al_{18}$	
Hardness	**Reference state**	**Charged**	**Reference state**	**Charged**	**Reference state**	**Charged**
Hardness (HRC)	44 ± 1[a]	44 ± 1	39 ± 1	39 ± 1	38 ± 1	38 ± 1
Microhardness (HV 0.1)	540 ± 20	570 ± 23	380 ± 19	435 ± 18	255 ± 14	430 ± 19

[a]Values are reported as mean ± standard deviation (SD).

15272648, 2026, 17, Downloaded from https://advanced.onlinelibrary.wiley.com/doi/10.1002/adem.202503163 by Universitaet Bayreuth, Wiley Online Library on [27/10/2026]. See the Terms and Conditions (https://onlinelibrary.wiley.com/terms-and-conditions) on Wiley Online Library for rules of use; OA articles are governed by the applicable Creative Commons License

increase is explained by hydrogen–dislocation interaction and reported to be related to the phenomenon of dislocation pinning [56, 60], enhanced dislocation evolution [55], and solid solution strengthening [55, 58]. Kirchheim [61] explains the hardening phenomenon related to hydrogen by the defectant concept, linking it to kink formation and motion at dislocations. The increase of hydrogen concentration in a material leads to its segregation at dislocations, creating hydrogen atmospheres. In this way, it pins the dislocations, thereby increasing the required stress for plastic deformations and leading to hydrogen-induced hardening [60]. This increase in hydrogen content is expected to occur underneath the indenter during hardness measurements at a level sufficient to create a Cottrell atmosphere [59].

The hardening effect of hydrogen was also reported for bcc Fe-based alloys [59, 62]. A gradual increase in hardness with charging time was observed during in situ nanoindentation tests, followed by a slow hardness decrease after charging stopped and hydrogen was effusing from the sample [59]. The observed change in hardness was thus attributed to the action of diffusive and weakly trapped hydrogen, leading to changes in dislocation density and friction stresses [59]. As the solubility of hydrogen in bcc Fe-based alloys is low [29, 59], only a limited amount of hydrogen can be accommodated in the single-phased solid solution alloy, so that the hydrogen-induced hardening effect in the $Fe_{65}Ni_{10}Al_{25}$ is the least pronounced. In two-phase alloys $Fe_{65}Ni_{15}Al_{20}$ and $Fe_{65}Ni_{17}Al_{18}$, precipitate-matrix interfaces act as traps for hydrogen, thereby facilitating the hardening effect. The comparison between microstructure and hardness values of both alloys shows that the $Fe_{65}Ni_{17}Al_{18}$ alloy, containing a higher fraction of precipitates as well as more coarsened precipitates, exhibits a more pronounced hardening effect. Precipitate coarsening in the Fe–Ni–Al system has been reported to promote the accumulation of dislocations at the matrix–precipitate interface [53]. This is supported by the observation of Rao et al. [59], where stronger hydrogen-induced hardening was reported for alloys with a higher content of alloying elements due to a higher amount of flat traps. As NiAl precipitates are known to possess a limited trapping ability [63–65], the hardening effect can also be attributed to diffusible hydrogen and dislocation interaction, similarly to [59, 60].

The absence of a noticeable effect of hydrogen charging on hardness, in contrast to its measurable effect on microhardness, can be rationalized by considering the measurement techniques. The HRC measurement technique operating with a higher force and a spheroconical indenter tip is known to be much less sensitive toward hydrogen-induced changes in hardness. Lee et al. [66] reported almost no changes in the hardness of low-carbon steel under various heat-treatment conditions after hydrogen charging, consistent with earlier results of Seabrook et al. [67] where no hardness increase was observed. It can be rationalized by considering the time required for hydrogen transport to the indentation zone. The duration of indenter penetration during HRC and HV 0.1 measurements is approximately the same according to instrument specifications. However, the corresponding penetration depths and thus the deformation rate differ significantly, being nearly two orders of magnitude larger for HRC measurements compared to HV 0.1. This implies a considerable difference in the diffusion process for hydrogen to diffuse to and accumulate at the elastically stressed region at the indenter tip according to the Gorsky effect [68, 69]. At the same time, it is well established from hydrogen–mechanical tests that lower deformation rates significantly enhance the effect of hydrogen [70].

3.2.2 | Strength

Mechanical properties of the alloys were assessed by three-point bending testing. The three-point-bending testing was specifically chosen over tensile testing in this case due to the brittle nature of the alloys. According to the Gorsky effect, hydrogen concentrates in regions of elastically stressed lattice, because elastic lattice distortions create energetically favorable sites for hydrogen [68, 69]. Thus, the bending test allows accumulating hydrogen in a localized area, where fracture is going to occur, and, in this way, intensifies the hydrogen influence on the brittle alloy. To analyze the test results, the force–deflection relations were averaged for each material for at least four specimens. The averaged force F – deflection f diagrams for the uncharged alloys are presented in Figure 2a. Based on these results, the averaged stress-strain σ–ε diagrams were obtained (Figure 2b).

As can be seen from the figure, the distinctive feature of the mechanical behavior of the alloys was their enhanced brittleness. The F–f diagrams are characterized by a linear behavior, preventing to record the yield strength. The F–f and σ–ε diagrams demonstrated no signs of macroplastic deformation of the alloys until failure, which allowed us to determine their strength R_m based on

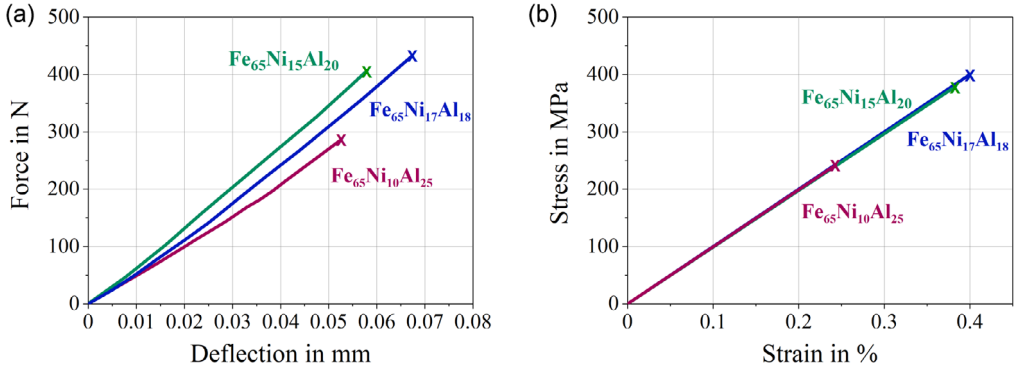


FIGURE 2 | Averaged force–deflection (F–f) and stress–strain (σ–ε) diagrams for $Fe_{65}Ni_{17}Al_{18}$, $Fe_{65}Ni_{15}Al_{20}$, and $Fe_{65}Ni_{10}Al_{25}$ alloys in the uncharged state. X marks the fracture of the specimen.

15272648, 2026, 17, Downloaded from https://advanced.onlinelibrary.wiley.com/doi/10.1002/adem.202503163 by Universitaet Bayreuth, Wiley Online Library on [27/10/2026]. See the Terms and Conditions (https://onlinelibrary.wiley.com/terms-and-conditions) on Wiley Online Library for rules of use; OA articles are governed by the applicable Creative Commons License

the maximum stress level: $R_m = 240$ MPa, 375 MPa, and 400 MPa for $Fe_{65}Ni_{10}Al_{25}$, $Fe_{65}Ni_{15}Al_{20}$, and $Fe_{65}Ni_{17}Al_{18}$, respectively. This behavior is considered to be a characteristic feature of this group of alloys at room temperature. For comparison, the mechanical behavior of conventional structural steels with similar hardness (HRC = 38–44) would exhibit noticeable plastic deformation regions, allowing for the determination of the yield strength [71].

Figure 3 shows the mechanical behavior of the alloys after cathodic hydrogen charging in the form of force–deflection *F–f* diagrams. The specimens presented here were charged at 10 and 20 mA/cm^2 for 48 or 72 h prior to being subjected to tree-point bending testing. With account for certain data scatter, the shaded data regions are presented in Figure 3, bounded by the minimal and maximal data curve, where the test results for each charging mode fall inside. To improve the figure readability and avoid data overlap, only these minimal and maximal data curves for each charging mode are shown, while the curves

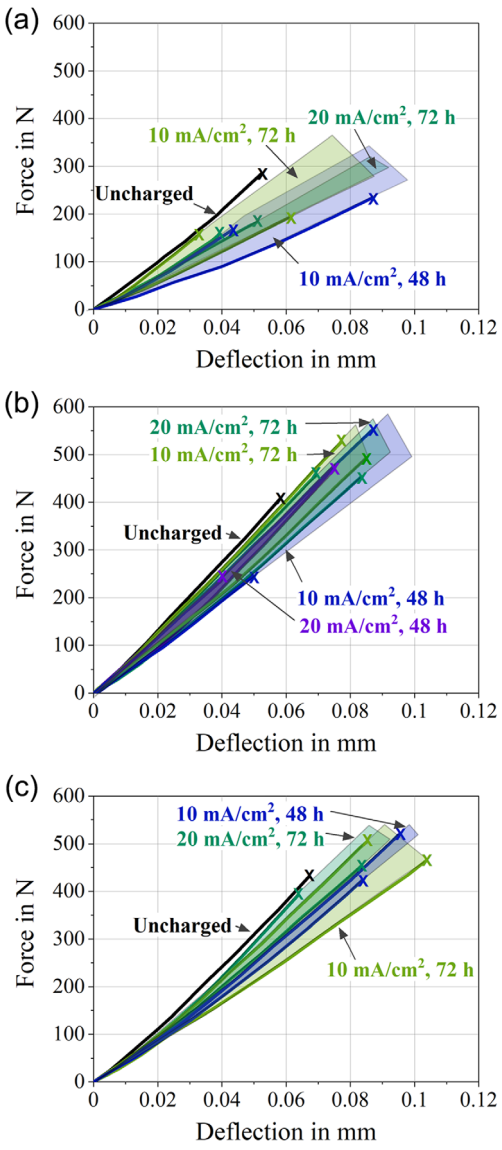


FIGURE 3 | Force-deflection *F–f* diagrams for the $Fe_{65}Ni_{10}Al_{25}$ (a), $Fe_{65}Ni_{15}Al_{20}$ (b), and $Fe_{65}Ni_{17}Al_{18}$ (c) alloys after hydrogen charging under different charging modes. *X* marks the fracture of the specimen.

lying inside each of the regions are omitted. For all alloys, it has been observed that the curve corresponding to the uncharged state is located with the highest inclination angle to the deflection axis, while the curves corresponding to the charged specimens lie underneath it. This means that for the same deflection value, a higher force is necessary for the specimen to fail in the uncharged state compared to the charged one. In addition, for the charged specimens of especially both two-phase alloys $Fe_{65}Ni_{15}Al_{20}$ and $Fe_{65}Ni_{17}Al_{18}$, in some cases, higher deflection values at failure were recorded as compared to the uncharged state. However, it should be noted that deflection reflects the compliance of the sample and therefore causes significant scatter in the data for such brittle alloys.

The observed scatter of experimental results after three-point bending testing can be explained by several reasons. First, in bcc transition metals, brittle fracture constitutes a principal failure mechanism [72]. The brittle behavior of the studied alloys is observed already in the reference state (Figure 2a) and partially accounts for the scatter observed in the experimental results after further embrittling of the alloys by the introduced hydrogen. Second, since the studied alloys were cast in the laboratory, despite careful selection of high-quality samples, the presence of internal casting defects, such as small cavities, cannot be excluded. Hydrogen, in its turn, is often trapped at defects, leading to hydrogen accumulation and thus higher hydrogen concentrations near the defects [23, 73], which influences the mechanical properties. Third, the sandwich structures of the two-phase alloys create an additional phase–matrix-interface, which is known to serve as a hydrogen trap [23].

The σ–ε diagrams averaged across all tested specimens for each charging mode (Figure 4) showed no significant change in the pattern of relations when compared with relations for the reference state for charged alloys. They remained linear and overlapped with the data for the reference state, with differences only in the quantitative values of the fracture stress. This indicates that, in contrast to the *F–f* diagrams, charging of the specimens had no significant effect on the Young's modulus of the studied alloys within the accuracy of the stress–strain diagram construction.

Table 3 summarizes the results of the effect of hydrogen charging on the strength of alloys for the different charging modes based on the averaged strength values. The alloy $Fe_{65}Ni_{10}Al_{25}$, the least strong alloy in its initial state with $R_m = 240$ MPa, is characterized by a further decrease in strength. This data clearly demonstrates the manifestation of hydrogen embrittlement. However, it should be noted that charging with a current density of 10 and 20 mA/cm^2 for the same duration of 72 h did not affect the R_m level.

Both two-phase alloys, $Fe_{65}Ni_{15}Al_{20}$ and $Fe_{65}Ni_{17}Al_{18}$, exhibiting higher strength, in general, do not significantly differ from each other in terms of the hydrogen effect after charging at 20 mA/cm^2. However, some opposing effects can be observed, i.e. an increase and a decrease in the strength of these alloys as a result of hydrogen charging. Statistical analysis of the experimental data based on standard deviation and standard error values confirms the reliability of the obtained data and conclusions, including the observed differences in strength. At the same time, instances where no statistically significant differences are

15272648, 2026, 17, Downloaded from https://advanced.onlinelibrary.wiley.com/doi/10.1002/adem.202503163 by Universitaet Bayreuth, Wiley Online Library on [27/10/2026]. See the Terms and Conditions (https://onlinelibrary.wiley.com/terms-and-conditions) on Wiley Online Library for rules of use; OA articles are governed by the applicable Creative Commons License

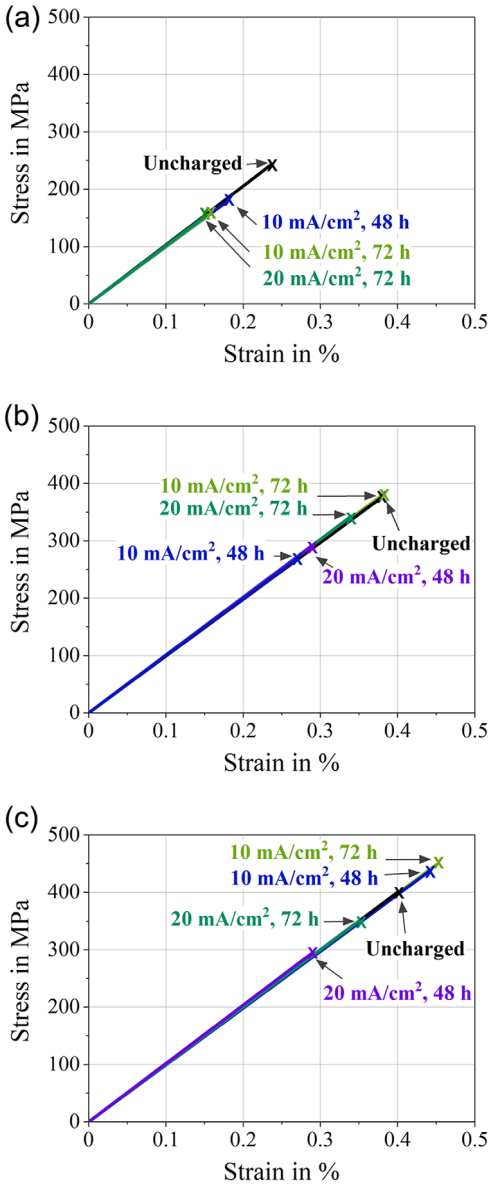


FIGURE 4 | Stress–strain σ–ε diagrams for the $Fe_{65}Ni_{10}Al_{25}$ (a), $Fe_{65}Ni_{15}Al_{20}$ (b), and $Fe_{65}Ni_{17}Al_{18}$ (c) alloys after hydrogen charging under different charging modes. *X* marks the fracture of the specimen.

observed are also noted, as indicated by the overlap of the experimental data (Figure 3). Here, the microstructure of the metal with increased brittleness and the presence of inclusions must be taken into account, which induces a decohesive mechanism of hydrogen influence with the formation of hydrogen traps as a result of micro-damage.

3.3 | Fractography Analysis

The tendencies observed during the mechanical testing are supported by the SEM images of fracture surfaces. The fracture surfaces of all three alloys, investigated in both charged and uncharged states, exhibit a brittle fracture pattern. A direct comparison of the charged and uncharged states is presented on the example of the $Fe_{65}Ni_{17}Al_{18}$ alloy. Figure 5 shows the fracture surface of the $Fe_{65}Ni_{17}Al_{18}$ alloy in the uncharged state. Figure 5a presents the general view of the specimen fracture surface, which is characterized by brittle, predominantly transcrystalline fracture with a few intercrystalline sites. Notably, there is a high proportion of fracture planes with varying orientation angles. The detailed examination of specific areas reveals clearly defined lines delimiting fracture structure (Figure 5b–d). Terraced structures are also present on the fracture surface, but only in certain individual areas.

Figure 6 presents a fracture surface of the $Fe_{65}Ni_{17}Al_{18}$ specimen after charging for 24 h at 10 mA/cm^2 current density. After charging, the $Fe_{65}Ni_{17}Al_{18}$ alloy exhibits a predominantly transcrystalline fracture along specific fracture surfaces. Compared to the uncharged state, the fracture surface of the charged sample presents significantly fewer fracture orientations. The fracture surface is dominated by parallelly arranged terraced structures, where each terrace reveals smaller terraces upon magnification. A detailed inspection of specific fracture regions reveals the presence of feather-like structures, gaping grain boundaries, secondary cracks in some areas, and hairlines on the grain boundary surfaces (Figure 6b–e), which are considered to be indicators of hydrogen influence on a material [68, 74, 75]. Despite being less prominently present, as compared to the more ductile materials [68, 76], these features confirm the hydrogen effect on the considered material.

3.4 | Generalized Strength–Hydrogen Concentration Relations

Figure 7 shows the fracture stress σ, characterizing the strength of alloys, for various hydrogen concentrations achieved by applying different charging modes for the alloys $Fe_{65}Ni_{10}Al_{25}$, $Fe_{65}Ni_{15}Al_{20}$, and $Fe_{65}Ni_{17}Al_{18}$. The vertical and horizontal dashed lines indicate the hydrogen concentration and the average fracture stress in reference specimens, respectively. As shown in the figure, the alloy $Fe_{65}Ni_{10}Al_{25}$ obtains a wider hydrogen concentration range after charging, while the increase in hydrogen concentration leads to a decrease in fracture force. Also, the strength of the charged samples of this alloy is the lowest. Alloy $Fe_{65}Ni_{17}Al_{18}$ also has a wide range of hydrogen concentrations depending on the hydrogenation mode. However, unlike the alloy $Fe_{65}Ni_{10}Al_{25}$, an increase in

TABLE 3 | Effect of hydrogen charging modes on the bending strength.

Alloy	R_m, MPa				
	Reference state	10 mA/cm², 48 h	10 mA/cm², 72 h	20 mA/cm², 48 h	20 mA/cm², 72 h
$Fe_{65}Ni_{10}Al_{25}$	240 ± 12/7[a]	180 ± 14/8	155 ± 8/5	180 ± 18/10	150 ± 10/6
$Fe_{65}Ni_{15}Al_{20}$	375 ± 18/10	270 ± 27/15	380 ± 34/20	290 ± 26/15	345 ± 28/16
$Fe_{65}Ni_{17}Al_{18}$	400 ± 16/9	435 ± 27/15	450 ± 18/10	295 ± 17/10	350 ± 30/17

[a]Values are reported as mean ± standard deviation (SD)/standard error (SE).

15272648, 2026, 17, Downloaded from https://advanced.onlinelibrary.wiley.com/doi/10.1002/adem.202503163 by Universitaet Bayreuth, Wiley Online Library on [27/10/2026]. See the Terms and Conditions (https://onlinelibrary.wiley.com/terms-and-conditions) on Wiley Online Library for rules of use; OA articles are governed by the applicable Creative Commons License

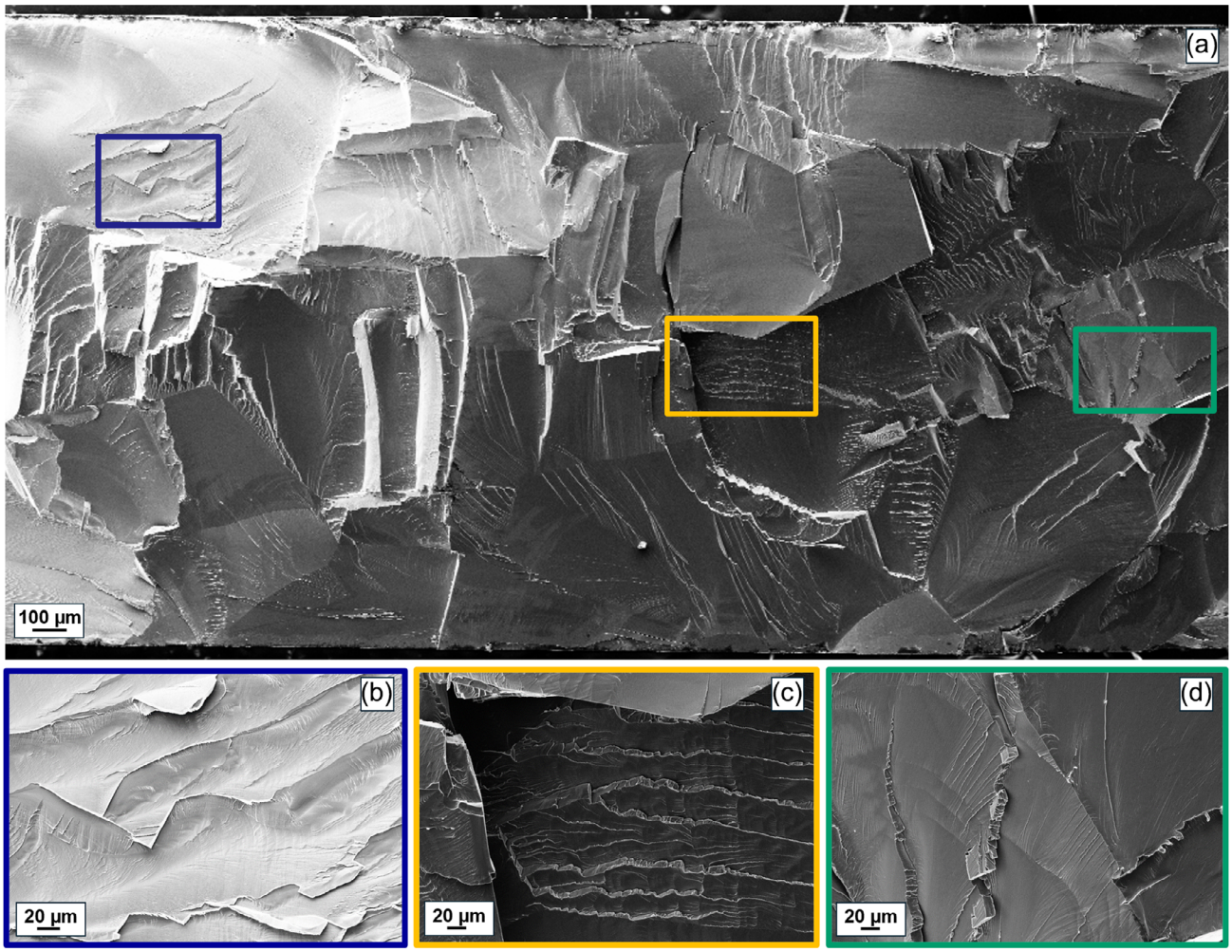


FIGURE 5 | SEM image of the fracture surface of $Fe_{65}Ni_{17}Al_{18}$ alloy in the uncharged state after the three-point bending testing: (a) the general view, (b–d) detailed views of the selected marked areas.

concentration in $Fe_{65}Ni_{17}Al_{18}$ and $Fe_{65}Ni_{15}Al_{20}$ alloys leads to a slight increase in fracture stress.

The investigated alloys are distinctive, also in terms of hydrogen influence, as they exhibit linear loading behavior until failure. Usually, materials tend to have a yield point, neck formation, and a final plastic deformation section of the sample, which makes it possible not only to distinguish between the ultimate and yield strength but also to observe the effect of hydrogen at different stages of deformation. The effect of hydrogen on such materials is usually concentrated in the areas of plastic deformation before and after neck formation. In our case, due to the absolutely brittle behavior of alloys, only the ultimate strength can be used as a mechanical parameter.

On the fundamental stress–concentration (σ–C_H) relations shown in Figure 7, the plot direction varies for different alloys. As for the $Fe_{65}Ni_{10}Al_{25}$ alloy with the lowest strength ($R_m = 240$ MPa) and maximum hardness in its initial state, the general tendency for strength decrease with increasing hydrogen concentration is observed, which is typical for the manifestation of hydrogen embrittlement. At the same time, the other alloys demonstrated the opposite trend in σ–C_H relations: an increase in hydrogen concentration increased strength. They also have a specific, high-energy-intensive fracture surface, which is overlaid by a physically determined manifestation of hydrogen embrittlement. It is reasonable to assume that until the strength in the initial state is reached ($R_m = 375$ and 400 MPa for $Fe_{65}Ni_{15}Al_{20}$ and $Fe_{65}Ni_{17}Al_{18}$ alloys, respectively), the typical hydrogen effect dominates, while further increasing the fracture energy intensity from the complex fracture surface morphology takes over.

According to the general assumptions, cleavage is considered to be the least energy-intensive form of fracture. Similar results were reported for pipeline steel under cathodic hydrogen charging, but the material exhibited greater ductility compared to the alloys studied, and the fracture mechanism was identified as transgranular quasi-cleavage [12]. However, low energy consumption is recorded for common crack growth, approximately in one plane, with no significant deviation. In our case, fractographic analysis revealed complex cleavage fracture topography despite crack growth in a single direction (Figure 6). This is a terraced-cascade and layered fracture, characterized by numerous areas of cleavage fracture, each of which is inherently low energy, but the resultant cumulative energy for all complexly oriented areas is high. Occasionally, secondary cracks perpendicular to the fracture surface were also

15272648, 2026, 17, Downloaded from https://advanced.onlinelibrary.wiley.com/doi/10.1002/adem.202503163 by Universitaet Bayreuth, Wiley Online Library on [27/10/2026]. See the Terms and Conditions (https://onlinelibrary.wiley.com/terms-and-conditions) on Wiley Online Library for rules of use; OA articles are governed by the applicable Creative Commons License

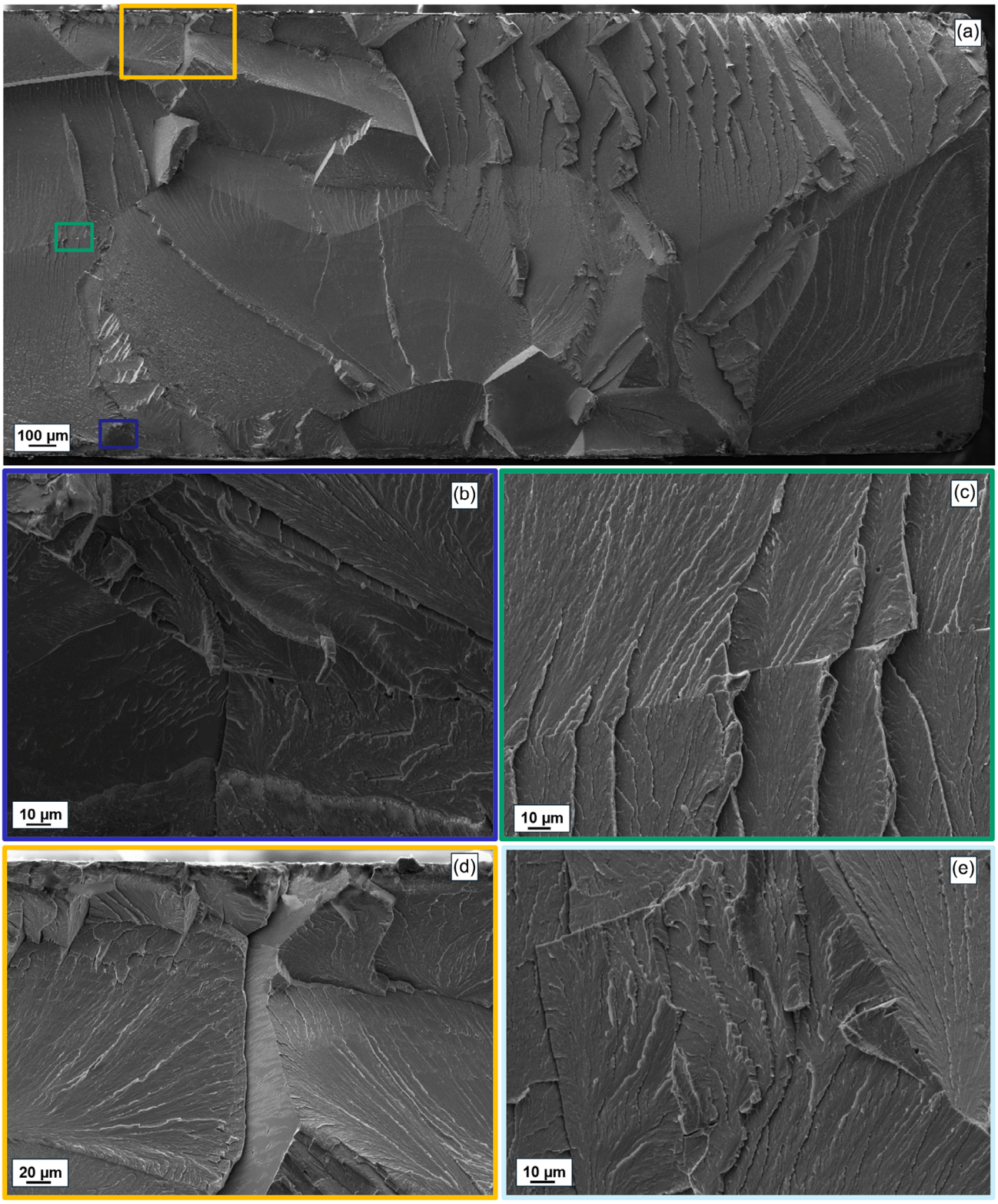


FIGURE 6 | SEM image of the fracture surface of $Fe_{65}Ni_{17}Al_{18}$ alloy charged for 24 h at 10 mA/cm^2 current density after the three-point bending testing: (a) the general view, (b–e) detailed views of selected marked areas, with e located outside of the image a.

detected (Figures 6b and 8), which creates the effect of crack branching with an increase in fracture energy. In this case, two counteracting processes are involved: facilitation of fracture by hydrogen embrittlement and hindrance by the complex geometry of the dominant fracture surface. This explains why an increase in hydrogen concentration increases strength.

Thus, the fracture mechanisms were analyzed from both a physical and a mechanical perspective. From a physical perspective, two mechanisms of hydrogen influence were considered. The first involved a reduction in cohesive strength, which was attributed to the single-phase alloy $Fe_{65}Ni_{10}Al_{25}$, with transgranular fracture occurring via a low-energy cleavage mechanism. The opposite

15272648, 2026, 17, Downloaded from https://advanced.onlinelibrary.wiley.com/doi/10.1002/adem.202503163 by Universitaet Bayreuth, Wiley Online Library on [27/10/2026]. See the Terms and Conditions (https://onlinelibrary.wiley.com/terms-and-conditions) on Wiley Online Library for rules of use; OA articles are governed by the applicable Creative Commons License

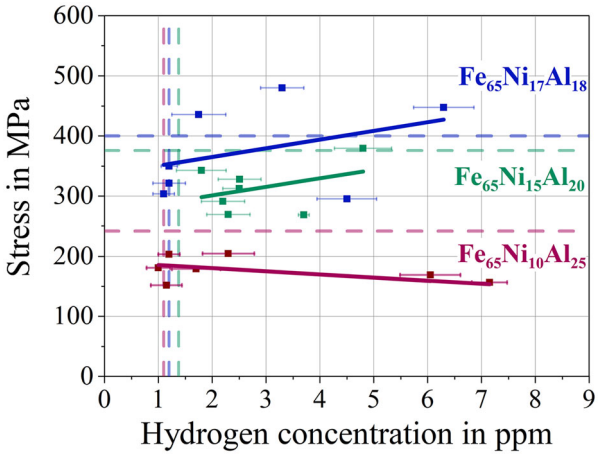


FIGURE 7 | Generalized fracture stress – hydrogen concentration relations for studied alloys. Dashed lines correspond to the concentration (vertical dashed lines) and stress (horizontal dashed lines) of the uncharged samples.

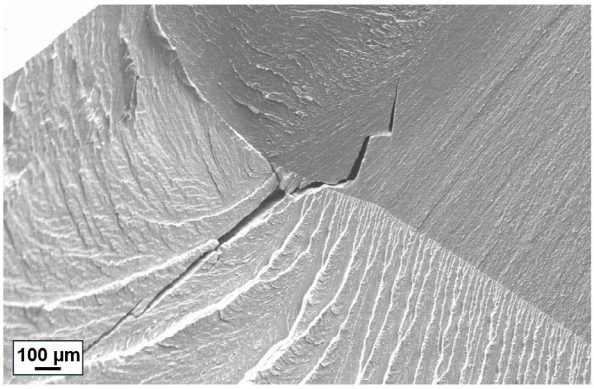


FIGURE 8 | SEM image of the fracture surface of hydrogen-charged $Fe_{65}Ni_{10}Al_{25}$ alloy for 96 h at 20 mA/cm^2 after the three-point bending testing.

trend was attributed to dislocation strengthening, i.e., the hydrogen-induced increase in dislocation density [59]. From a mechanical perspective, the mechanism of strength increase with rising hydrogen concentration was analyzed in two-phase alloys. Hydrogen intensifies multiple fractures, also governed by a cleavage mechanism, which is more significantly pronounced with increasing hydrogen concentration. This acted as a contributing factor to the increase in multiple fracture energy due to the sum of the energies associated with elementary low-energy cleavage fractures.

4 | Conclusion

- Through variation in nickel and aluminum content, distinct microstructures of iron-based alloys were obtained: a single-phased $Fe_{65}Ni_{10}Al_{25}$ (in at-%) and two-phased precipitated strengthened $Fe_{65}Ni_{15}Al_{20}$ and $Fe_{65}Ni_{17}Al_{18}$. These microstructural differences were found to have a significant influence on the resulting material properties in the reference state and after hydrogen charging.
- The force–deflection curves obtained from three-point bending tests of all alloys exhibited linear behavior up to fracture, indicating a purely brittle response without any observable yielding or measurable yield strength.
- The samples were electrochemically charged for 24–96 h at cathode current densities of 10 and 20 mA/cm^2. These charging conditions ensure the absence of hydrogen blistering. The specimens in their initial uncharged state contained a baseline average hydrogen concentration of 1.1–1.4 ppm. Under the applied charging conditions, the measured hydrogen concentrations in the investigated alloys increased up to 7.2 ppm.
- Preliminary hydrogen charging did not affect the hardness of the alloys. However, a distinct influence on the microhardness of the alloys was observed: the harder one-phase alloy $Fe_{65}Ni_{10}Al_{25}$ exhibited a slight decrease in HV 0.1, whereas the two-phase alloys $Fe_{65}Ni_{15}Al_{20}$ and $Fe_{65}Ni_{17}Al_{18}$ showed a strong increase. This effect can be explained by hydrogen–dislocation interaction due to diffusible hydrogen.
- The single-phase alloy $Fe_{65}Ni_{10}Al_{25}$, the weakest in its initial state ($R_m = 240$ MPa), experienced a further reduction in strength under hydrogen exposure, likely due to diffusible hydrogen. The two-phase alloys $Fe_{65}Ni_{15}Al_{20}$ and $Fe_{65}Ni_{17}Al_{18}$, which exhibited higher initial strength, showed similar, less pronounced hydrogen effects. The presence of precipitates in the microstructure promotes a decohesive hydrogen effect, forming hydrogen traps through micro-damage and indicating a different mechanism of hydrogen interaction.
- The investigated alloys exhibit predominantly transgranular cleavage fracture, typically considered the least energy-intensive fracture mode. However, multiple cleavages along terraced, cascaded, layered paths are common, resulting in a high cumulative fracture energy across complexly oriented regions. Hydrogenation enhances this complex fracture behavior in two-phase alloys, which is reflected in an increase in strength with increasing hydrogen concentration. Therefore, the effect of hydrogen on the strength of these alloys arises from two opposing factors: the physically driven manifestation of hydrogen influence and the mechanically driven increase in fracture energy due to the complex fracture surface topography.

Author Contributions

Nataliya Yadzhak: conceptualization (lead), formal analysis (equal), funding acquisition (lead), investigation (lead), methodology (equal), project administration (lead), visualization (lead), writing – original draft (lead), writing – review & editing (equal). **Olha Zvirko**: conceptualization (supporting), funding acquisition (supporting), project administration (supporting), writing – review & editing (equal). **Rostyslav Leshchak**: formal analysis (equal), investigation (equal), methodology (equal), writing – review & editing (equal). **Hryhoriy Nykyforchyn**: conceptualization (equal), formal analysis (equal), methodology (equal), project administration (supporting), writing – original draft (lead), writing – review & editing (equal).

Acknowledgments

Nataliya Yadzhak is sincerely grateful to Prof. Dr.-Ing. Uwe Glatzel for his support and mentorship at the Chair for Metals and Alloys at the

15272648, 2026, 17, Downloaded from https://advanced.onlinelibrary.wiley.com/doi/10.1002/adem.202503163 by Universitaet Bayreuth, Wiley Online Library on [27/10/2026]. See the Terms and Conditions (https://onlinelibrary.wiley.com/terms-and-conditions) on Wiley Online Library for rules of use; OA articles are governed by the applicable Creative Commons License

University of Bayreuth, as well as to Dr.-Ing. Florian Scherm for his valuable remarks on this manuscript.

Open Access funding enabled and organized by Projekt DEAL.

Funding

Nataliya Yadzhak: This project has received funding through the MSCA4Ukraine project, which is funded by the European Union. Views and opinions expressed are however those of the author(s) only and do not necessarily reflect those of the European Union. Neither the European Union nor the MSCA4Ukraine Consortium as a whole nor any individual member institutions of the MSCA4Ukraine Consortium can be held responsible for them. **Olha Zvirko & Hryhoriy Nykyforchyn**: Partial financial support was received from the National Academy of Sciences of Ukraine under R&D project (Registration No. 0124U0000911).

Conflicts of Interest

The authors declare no conflicts of interest.

Data Availability Statement

The data that support the findings of this study are available from the corresponding author upon reasonable request.

References

1. R. C. Reed, *The Superalloys: Fundamentals and Applications*, (Cambridge Univ. Press, 2006).

2. M. Müller, H. J. Stone, E. Galindo-Nava, et al., "Microstructure-Based Modeling of Temperature-Dependent Yield Strength in Polycrystalline Ni-Based Superalloys," in Superalloys, 2024: Proceedings of the, 15th International Symposium on Superalloys, eds. J. Cormier, I. Edmonds, S. Forsik et al., (Springer, 2024), 412–424, https://doi.org/10.1007/978-3-031-63937-1_39.

3. M. Zamanzade and A. Barnoush, "An Overview of the Hydrogen Embrittlement of Iron Aluminides," *Procedia Materials Science* 3 (2014): 2016–2023, https://doi.org/10.1016/j.mspro.2014.06.325.

4. K. Ma, P. A. Ferreirós, T. W. Pfeifer, et al., "Intermetallic Dispersion-Strengthened Ferritic Superalloys with Exceptional Resistance to Radiation-Induced Hardening," *Acta Materialia* 293 (2025): 121095, https://doi.org/10.1016/j.actamat.2025.121095.

5. L. Á. Morales, A. Bezold, A. Förner, et al., "Influence of Cu Addition and Microstructural Configuration on the Creep Resistance and Mechanical Properties of an Fe-Based α/α′/α″ Superalloy," *Advanced Engineering Materials* 25, no. 9 (2023): 2201652, https://doi.org/10.1002/adem.202201652.

6. A. J. Knowles and C. H. Zenk, "BCC-Superalloys: Perspectives and Challenges," *Scripta Materialia* 267 (2025): 116761, https://doi.org/10.1016/j.scriptamat.2025.116761.

7. Q. Wang, Z. Wang, R. Wang, et al., "Mechanical Behavior of BCC-Superalloys," *Scripta Materialia* 267 (2025): 116748, https://doi.org/10.1016/j.scriptamat.2025.116748.

8. P. Liaw, G. Ghosh, M. Asta, M. Fine, and C. Liu, *Computational Design and Prototype Evaluation of Aluminide-Strengthened Ferritic Superalloys for Power-Generating Turbine Applications up to 1,033 K* (Univ. of Tennessee, 2010).

9. N. Q. Vo, C. H. Liebscher, M. J. Rawlings, M. Asta, and D. C. Dunand, "Creep Properties and Microstructure of a Precipitation-Strengthened Ferritic Fe–Al–Ni–Cr Alloy," *Acta Materialia* 71 (2014): 89–99, https://doi.org/10.1016/j.actamat.2014.02.020.

10. O. Nagel, M. Fritton, A. Mutschke, et al., "Impact of High-Pressure Hydrogen Charging on Mechanical Behavior and Lattice Parameters of a Polycrystalline CoNiCr-Based Superalloy," *Scripta Materialia* 260 (2025): 116594, https://doi.org/10.1016/j.scriptamat.2025.116594.

11. H. Krechkovska, O. Student, O. Zvirko, et al., "Substantiation of the Critical Structural and Mechanical State of Low-Alloy Heat-Resistant Steel from Steam Pipelines of Thermal Power Plant," *Engineering Failure Analysis* 150 (2023): 107359, https://doi.org/10.1016/j.engfailanal.2023.107359.

12. J. L. Gonzalez-Velázquez, E. Entezari, D. R. López, M. A. B. Zúñiga, and J. Szpunar, "Experimental and In-Service Observations of HIC Nucleation and Growth in Pipeline Steel," *Quantitative Nondestructive Evaluation* 49 (2022): 171, https://doi.org/10.1115/QNDE2022-97160.

13. V. G. Rivlin and G. V. Raynor, "2: Critical Evaluation of Constitution of Aluminium-Iron-Nickel System," *International Metals Reviews* 25, no. 1 (2013): 79–93, https://doi.org/10.1179/imtr.1980.25.1.79.

14. V. Raghavan, "Al-Fe-Ni (Aluminum-Iron-Nickel)," *Journal of Phase Equilibria* 15, no. 4 (1994): 411–413, https://doi.org/10.1007/BF02647565.

15. V. Raghavan, "Al-Fe-Ni (Aluminum-Iron-Nickel)," *Journal of Phase Equilibria and Diffusion* 27, no. 5 (2006): 489–490, https://doi.org/10.1007/BF02736451.

16. G. Sauthoff, "Multiphase Intermetallic Alloys for Structural Applications," *Intermetallics* 8, no. 9–11 (2000): 1101–1109, https://doi.org/10.1016/S0966-9795(00)00045-5.

17. L. Zhang, J. Wang, Y. Du, et al., "Thermodynamic Properties of the Al–Fe–Ni System Acquired via a Hybrid Approach Combining Calorimetry, First-Principles and CALPHAD," *Acta Materialia* 57, no. 18 (2009): 5324–5341, https://doi.org/10.1016/j.actamat.2009.07.031.

18. L. Eleno, K. Frisk, and A. Schneider, "Assessment of the Fe–Ni–Al System," *Intermetallics* 14, no. 10–11 (2006): 1276-1290, https://doi.org/10.1016/j.intermet.2005.11.021.

19. E. Contreras-Piedras, H. J. Dorantes-Rosales, V. M. López-Hirata, et al., "Analysis of Precipitation in Fe-Rich Fe–Ni–Al Alloys by Diffusion Couples," *Materials Science and Engineering: A* 558 (2012): 366–370, https://doi.org/10.1016/j.msea.2012.08.013.

20. M. A. Muñoz-Morris and D. G. Morris, "Microstructure and Mechanical Behaviour of a Fe–Ni–Al Alloy," *Materials Science and Engineering: A* 444, no. 1–2 (2007): 236–241, https://doi.org/10.1016/j.msea.2006.08.082.

21. H. J. Dorantes-Rosales, V. M. Lopez-Hirata, J. L. Gonzalez-Velazquez, N. Cayetano-Castro, and M. L. Saucedo-Muñoz, "Precipitation Process in Fe-Ni-Al-Based Alloys," in *Superalloys*, ed. M. Aliofkhazraei, Ch. 4, (IntechOpen, 2015). https://doi.org/10.5772/61070.

22. Z. K. Teng, C. T. Liu, M. K. Miller, et al., "Room Temperature Ductility of NiAl-Strengthened Ferritic Steels: Effects of Precipitate Microstructure," *Materials Science and Engineering: A* 541 (2012): 22–27, https://doi.org/10.1016/j.msea.2012.01.103.

23. S. Lynch, "Hydrogen Embrittlement Phenomena and Mechanisms," *Corrosion Reviews* 30, no. 3–4 (2012): 105–123, https://doi.org/10.1515/corrrev-2012-0502.

24. Y.-S. Chen, C. Huang, P.-Y. Liu, et al., "Hydrogen Trapping and Embrittlement in Metals – A Review," *International Journal of Hydrogen Energy* 136 (2025): 789–821, https://doi.org/10.1016/j.ijhydene.2024.04.076.

25. H. Yu, A. Díaz, X. Lu, et al., "Hydrogen Embrittlement as a Conspicuous Material Challenge – Comprehensive Review and Future Directions," *Chemical Reviews* 124, no. 10 (2024): 6271–6392, https://doi.org/10.1021/acs.chemrev.3c00624.

26. A. Pundt and R. Kirchheim, "Hydrogen in Metals: Microstructural Aspects," *Annual Review of Materials Research* 36, no. 1 (2006): 555–608, https://doi.org/10.1146/annurev.matsci.36.090804.094451.

27. R. Kirchheim and A. Pundt, "Hydrogen in Metals," in *Physical Metallurgy*, Fifth Edition, ed. D. E. Laughlin and K. Hono (Elsevier, 2014), 2597–2705.

15272648, 2026, 17, Downloaded from https://advanced.onlinelibrary.wiley.com/doi/10.1002/adem.202503163 by Universitaet Bayreuth, Wiley Online Library on [27/10/2026]. See the Terms and Conditions (https://onlinelibrary.wiley.com/terms-and-conditions) on Wiley Online Library for rules of use; OA articles are governed by the applicable Creative Commons License

28. V. G. Gavriljuk, V. M. Shyvaniuk, and S. M. Teus, *Hydrogen in Engineering Metallic Materials: From Atomic-Level Interactions to Mechanical Properties*, (Springer Cham, 2022).

29. M. Nagumo, *Fundamentals of Hydrogen Embrittlement*, (Springer, 2023).

30. Y. Murakami and S. Matsuoka, "Effect of Hydrogen on Fatigue Crack Growth of Metals," *Engineering Fracture Mechanics* 77, no. 11 (2010): 1926–1940, https://doi.org/10.1016/j.engfracmech.2010.04.012.

31. W. H. Johnson and W. Thomson, "II. On Some Remarkable Changes Produced in Iron and Steel by the Action of Hydrogen and Acids," *Proceedings of the Royal Society of London* 23, no. 156–163 (1875): 168–179, https://doi.org/10.1098/rspl.1874.0024.

32. V. G. Gavriljuk, B. D. Shanina, V. N. Shyvanyuk, and S. M. Teus, "Electronic Effect on Hydrogen Brittleness of Austenitic Steels," *Journal of Applied Physics* 108, no. 8 (2010): 083723, https://doi.org/10.1063/1.3499610.

33. T. Michler and J. Naumann, "Hydrogen Environment Embrittlement of Austenitic Stainless Steels at Low Temperatures," *International Journal of Hydrogen Energy* 33, no. 8 (2008): 2111–2122, https://doi.org/10.1016/j.ijhydene.2008.02.021.

34. M. L. Martin, M. J. Connolly, F. W. DelRio, and A. J. Slifka, "Hydrogen Embrittlement in Ferritic Steels," *Applied Physics Reviews* 7, no. 4 (2020): 041301, https://doi.org/10.1063/5.0012851.

35. E. Entezari, J. L. V. González, D. R. López, et al., "Experimental Study on Hydrogen Embrittlement Behavior of X80 and X70 Pipeline Steels Evaluated by Hydrogen Permeation and Slow Strain Rate Tensile Tests," *Journal of Failure Analysis and Prevention* 24, no. 6 (2024): 2900–2911, https://doi.org/10.1007/s11668-024-02042-1.

36. D. Kniep, S. Schewe, M. Rudolphi, and M. C. Galetz, "Hydrogen Permeation and Embrittlement Behavior of Ferritic SOEC/SOFC Interconnect Candidates," *International Journal of Hydrogen Energy* 136 (2025): 843–851, https://doi.org/10.1016/j.ijhydene.2024.03.337.

37. S. Pichler, A. Bendo, G. Mori, M. Safyari, and M. Moshtaghi, "Inhibition of Grain Growth by Pearlite Improves Hydrogen Embrittlement Susceptibility of the Ultra-Low Carbon Ferritic Steel: The Influence of H-Assisted Crack Initiation and Propagation Mechanisms," *Journal of Materials Science* 58, no. 33 (2023): 13460–13475, https://doi.org/10.1007/s10853-023-08856-y.

38. E. Entezari, A. K. Singh, H. Mousavi, J. L. G. Velazquez, and J. Szpunar, "A Cost-Effective Model for Synergistic Effects of Microstructure and Crystallographic Texture on Hydrogen-Induced Crack Growth and Corrosion Rates in Pipeline Steels," *Materials Characterization* 223 (2025): 114917, https://doi.org/10.1016/j.matchar.2025.114917.

39. D. P. Escobar, T. Depover, L. Duprez, K. Verbeken, and M. Verhaege, "Combined Thermal Desorption Spectroscopy, Differential Scanning Calorimetry, Scanning Electron Microscopy and X-Ray Diffraction Study of Hydrogen Trapping in Cold Deformed TRIP Steel," *Acta Materialia* 60, no. 6-7 (2012): 2593-2605, https://doi.org/10.1016/j.actamat.2012.01.026.

40. P. Hammer, O. E. Peil, A. Azizpour, et al., "The Fingerprint Method for Analysis of Thermal Desorption Spectra," *npj Materials Degradation* 10, no. 1 (2026): 7, https://doi.org/10.1038/s41529-025-00718-z.

41. E. van den Eeckhout, K. Verbeken, and T. Depover, "Methodology of the Electrochemical Hydrogen Permeation Test: A Parametric Evaluation," *International Journal of Hydrogen Energy* 48, no. 78 (2023): 30585–30607, https://doi.org/10.1016/j.ijhydene.2023.04.211.

42. N. Saintier, T. Awane, J. M. Olive, S. Matsuoka, and Y. Murakami, "Analyses of Hydrogen Distribution around Fatigue Crack on type 304 Stainless Steel Using Secondary Ion Mass Spectrometry," *International Journal of Hydrogen Energy* 36, no. 14 (2011): 8630–8640, https://doi.org/10.1016/j.ijhydene.2011.03.111.

43. B. Gault, A. Saksena, X. Sauvage, et al., "Towards Establishing Best Practice in the Analysis of Hydrogen and Deuterium by Atom Probe Tomography," *Microscopy and Microanalysis* 30, no. 6 (2024): 1205–1220, https://doi.org/10.1093/mam/ozae081.

44. Y.-S. Chen, P.-Y. Liu, R. Niu, et al., "Atom Probe Tomography for the Observation of Hydrogen in Materials: A Review," *Microscopy and Microanalysis* 29, no. 1 (2023): 1–15, https://doi.org/10.1093/micmic/ozac005.

45. E. Entezari, J. L. G. Velázquez, M. A. Mohtadi-Bonab, et al., "Experimental Observations of Nucleation and Crack Growth Paths of Hydrogen-Induced Cracking in Pipeline Steel," *Engineering Failure Analysis* 154 (2023): 107650, https://doi.org/10.1016/j.engfailanal.2023.107650.

46. G. Wang, Y. Yan, X. Yang, J. Li, and L. Qiao, "Investigation of Hydrogen Evolution and Enrichment by Scanning Kelvin Probe Force Microscopy," *Electrochemistry Communications* 35 (2013): 100–103, https://doi.org/10.1016/j.elecom.2013.08.006.

47. DIN German Institute for Standardization, "Metallic Materials - Rockwell Hardness Test - Part 1: Test Method (ISO 6508-1:2023)".

48. DIN German Institute for Standardization, "Metallic Materials - Vickers Hardness Test - Part 1: Test Method (ISO 6507-1:2023)".

49. DIN German Institute for Standardization, "Metallic Materials - Bend Test (ISO 7438:2020)".

50. M. A. Muñoz-Morris, N. Calderon, and D. G. Morris, "Coarsening Kinetics of Metastable Nanoprecipitates in a Fe–Ni–Al Alloy," *Journal of Materials Science* 43, no. 10 (2008): 3674–3682, https://doi.org/10.1007/s10853-008-2589-y.

51. C. Stallybrass and G. Sauthoff, "Ferritic Fe–Al–Ni–Cr Alloys with Coherent Precipitates for High-Temperature Applications," *Materials Science and Engineering: A* 387–389 (2004): 985–990, https://doi.org/10.1016/j.msea.2004.01.108.

52. L. A. Morales, N. Luo, K. Li, C. H. Zenk, and C. Körner, "On Stabilizing an α/α′/α″ Microstructure in Ferritic Superalloys," *Journal of Alloys and Compounds* 911 (2022): 164996, https://doi.org/10.1016/j.jallcom.2022.164996.

53. C. Ferreira-Palma, E. Contreras-Piedras, N. Cayetano-Castro, et al., "Effect of Temperature and Composition on NiAl Precipitation and Morphology in Fe-Ni-Al Alloys," *Metallurgical and Materials Transactions A* 48, no. 11 (2017): 5285–5293, https://doi.org/10.1007/s11661-017-4309-1.

54. Y. Bai, J. Zhou, J. Li, and Z. Yang, "B2-Ordered NiAl Content on Microstructure, Mechanical and Oxidation Properties of FeAl Intermetallic Compounds," *Journal of Materials Research and Technology* 16 (2022): 1875–1888, https://doi.org/10.1016/j.jmrt.2021.12.128.

55. K. Wada, J. Yamabe, and H. Matsunaga, "Mechanism of Hydrogen-Induced Hardening in Pure Nickel and in a Copper–nickel Alloy Analyzed by Micro Vickers Hardness Testing," *Materials Science and Engineering: A* 805 (2021): 140580, https://doi.org/10.1016/j.msea.2020.140580.

56. Y. Murakami, T. Kanezaki, and Y. Mine, "Hydrogen Effect against Hydrogen Embrittlement," *Metallurgical and Materials Transactions A* 41, no. 10 (2010): 2548–2562, https://doi.org/10.1007/s11661-010-0275-6.

57. Y. Hong, C. Zhou, Y. Zheng, et al., "Dependence of Strain Rate on Hydrogen-Induced Hardening of Austenitic Stainless Steel Investigated by Nanoindentation," *International Journal of Hydrogen Energy* 44, no. 26 (2019): 14055–14063, https://doi.org/10.1016/j.ijhydene.2019.03.250.

58. Y. Zhao, D.-H. Lee, J.-A. Lee, et al., "Hydrogen-Induced Nanohardness Variations in a CoCrFeMnNi High-Entropy Alloy," *International Journal of Hydrogen Energy* 42, no. 16 (2017): 12015–12021, https://doi.org/10.1016/j.ijhydene.2017.02.061.

59. J. Rao, S. Lee, G. Dehm, and M. J. Duarte, "Hardening Effect of Diffusible Hydrogen on BCC Fe-Based Model Alloys by In Situ

15272648, 2026, 17, Downloaded from https://advanced.onlinelibrary.wiley.com/doi/10.1002/adem.202503163 by Universitaet Bayreuth, Wiley Online Library on [27/10/2026]. See the Terms and Conditions (https://onlinelibrary.wiley.com/terms-and-conditions) on Wiley Online Library for rules of use; OA articles are governed by the applicable Creative Commons License

Backside Hydrogen Charging," *Materials & Design* 232 (2023): 112143, https://doi.org/10.1016/j.matdes.2023.112143.

60. Y. Zhao, M.-Y. Seok, I.-C. Choi, et al., "The Role of Hydrogen in Hardening/Softening Steel: Influence of the Charging Process," *Scripta Materialia* 107 (2015): 46–49, https://doi.org/10.1016/j.scriptamat.2015.05.017.

61. R. Kirchheim, "Solid Solution Softening and Hardening by Mobile Solute Atoms with Special Focus on Hydrogen," *Scripta Materialia* 67, no. 9 (2012): 767–770, https://doi.org/10.1016/j.scriptamat.2012.07.022.

62. J. Hou, D. Peng, X.-S. Kong, et al., "Hydrogen Modulated Dislocation Reaction and Defect Accumulation in Bcc Metals," *Acta Materialia* 301 (2025): 121524, https://doi.org/10.1016/j.actamat.2025.121524.

63. J. Bestautte, A. Oudriss, M. Lenci, et al., "A Multi-Method Approach to the Study of Hydrogen Trapping in a Maraging Stainless Steel: The Impact of B2-NiAl Precipitates and Austenite," *Corrosion Science* 224 (2023): 111509, https://doi.org/10.1016/j.corsci.2023.111509.

64. C. Rousseau, A. Oudriss, R. Milet, et al., "Effect of Aging Treatment on Apparent Hydrogen Solubility and Trapping in a New Generation Maraging Steel," *Scripta Materialia* 183 (2020): 144–148, https://doi.org/10.1016/j.scriptamat.2020.03.013.

65. Y. Ma, Y. Shi, H. Wang, et al., "A First-Principles Study on the Hydrogen Trap Characteristics of Coherent Nano-Precipitates in α-Fe," *International Journal of Hydrogen Energy* 45, no. 51 (2020): 27941–27949, https://doi.org/10.1016/j.ijhydene.2020.07.123.

66. S.-J. Lee, J. A. Ronevich, G. Krauss, and D. K. Matlock, "Hydrogen Embrittlement of Hardened Low-Carbon Sheet Steel," *ISIJ International* 50, no. 2 (2010): 294–301, https://doi.org/10.2355/isijinternational.50.294.

67. J. B. Seabrook, N. J. Grant, and D. Carney, "Hydrogen Embrittlement of SAE. 1020 Steel," *JOM* 2, no. 11 (1950): 1317–1321, https://doi.org/10.1007/BF03399153.

68. J. Jürgensen and M. Pohl, "Impact and Detection of Hydrogen in Metals," *HTM Journal of Heat Treatment and Materials* 78, no. 5 (2023): 257–275, https://doi.org/10.1515/htm-2023-0020.

69. W. S. Gorsky, "Theorie der Elastischen Nachwirkung in Ungeordneten Mischkristallen (elastische Nachwirkung Zweiter Art)," *Physikalische Zeitschrift der Sowjetunion* 8 (1935): 457–471.

70. T. Depover, D. P. Escobar, E. Wallaert, Z. Zermout, and K. Verbeken, "Effect of Hydrogen Charging on the Mechanical Properties of Advanced High Strength Steels," *International Journal of Hydrogen Energy* 39, no. 9 (2014): 4647–4656, https://doi.org/10.1016/j.ijhydene.2013.12.190.

71. G. Bolzon, B. Rivolta, H. Nykyforchyn, and O. Zvirko, "Mechanical Analysis at Different Scales of Gas Pipelines," *Engineering Failure Analysis* 90 (2018): 434–439, https://doi.org/10.1016/j.engfailanal.2018.04.008.

72. L. Zhang, G. Csányi, E. van der Giessen, and F. Maresca, "Atomistic Fracture in Bcc Iron Revealed by Active Learning of Gaussian Approximation Potential," *npj Computational Materials* 9, no. 1 (2023): 217, https://doi.org/10.1038/s41524-023-01174-6.

73. X. Xing, Z. Pang, H. Zhang, J. Liu, and G. Cui, "Study of Temperature Effect on Hydrogen Embrittlement in X70 Pipeline Steel," *Corrosion Science* 230 (2024): 111939, https://doi.org/10.1016/j.corsci.2024.111939.

74. J. Flügge, ed., *Erscheinungsformen von Rissen und Brüchen metallischer Werkstoffe: the Appearance of Cracks and Fractures in Metallic Materials*, (Verl. Stahleisen, 2012).

75. G. Lange, "Schäden Durch Wasserstoff," in *Systhematische Beurteilung technischer Schadensfälle*, ed. G. Lange (WILEY-VCH, 2001), 255–275.

76. D. Kniep, M. Rudolphi, K. Ohla, A. Frehn, and M. C. Galetz, "Hydrogen Diffusivity, Solubility, and Embrittlement of High-Strength Copper Alloys in Comparison to Stainless Steel," *npj Materials Degradation* 9, no. 1 (2025): 56, https://doi.org/10.1038/s41529-025-00608-4.

15272648, 2026, 17, Downloaded from https://advanced.onlinelibrary.wiley.com/doi/10.1002/adem.202503163 by Universitaet Bayreuth, Wiley Online Library on [27/10/2026]. See the Terms and Conditions (https://onlinelibrary.wiley.com/terms-and-conditions) on Wiley Online Library for rules of use; OA articles are governed by the applicable Creative Commons License